USGS
science for a changing world

Calibration of the U.S. Geological Survey National Crustal Model

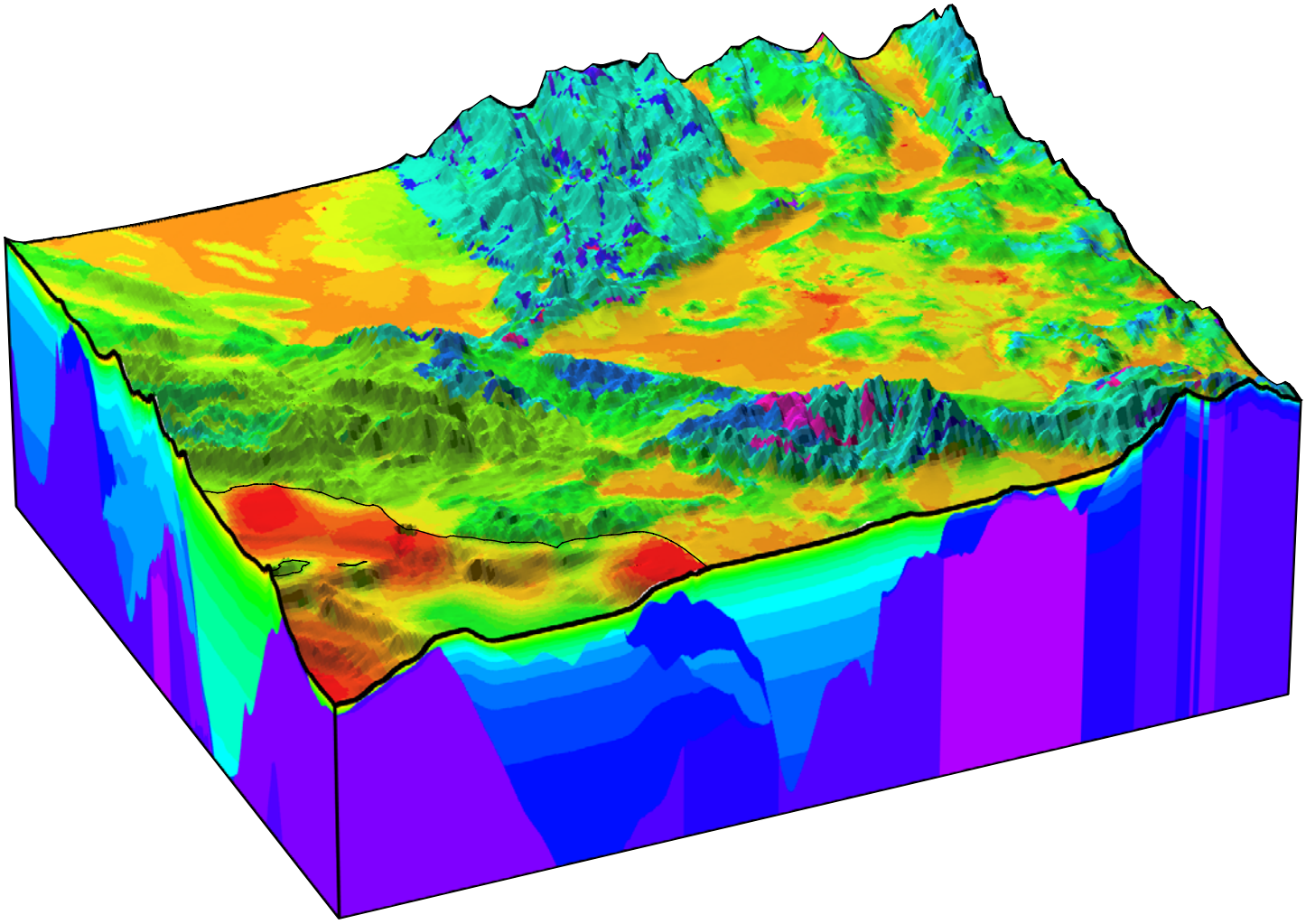

Open-File Report 2020–1052

U.S. Department of the Interior
U.S. Geological Survey

Cover. Shear-wave-velocity cross sections in southern California, from south to north, on the basis of the calibrations in this report and the related geologic framework. The time-averaged shear-wave velocity in the upper 30 meters is shown on top with a color scale that ranges between 100 and 1,000 meters per second. On the sides, shear-wave velocities extend to 10-kilometer depth with a vertical exaggeration of 10 times and have a color scale that ranges between 100 and 5,000 meters per second (Image created using calibrations in this report and the National Crustal Model geologic framework, v1.0.)

Calibration of the U.S. Geological Survey National Crustal Model

By Oliver S. Boyd

Open-File Report 2020–1052

U.S. Department of the Interior
U.S. Geological Survey

U.S. Department of the Interior
DAVID BERNHARDT, Secretary

U.S. Geological Survey
James F. Reilly II, Director

U.S. Geological Survey, Reston, Virginia: 2020

Suggested citation:
Boyd, O.S., 2020, Calibration of the U.S. Geological Survey National Crustal Model: U.S. Geological Survey Open-File Report 2020–1052, 23 p., https://doi.org/10.3133/ofr20201052.

Associated data for this publication:
Boyd, O.S., 2020a, Calibration coefficients for the U.S. Geological Survey National Crustal Model and depth to water table: U.S. Geological Survey data release, https://doi.org/10.5066/P9GO3CP8.

ISSN 2331-1258 (online)

Acknowledgments

I am grateful to the many colleagues and scientists that provided the information on which this work is based. Sean Ahdi at the University of Southern California, Domniki Asimaki at the California Institute of Technology, Albert Kottke at Pacific Gas and Electric, and Dave Boore, Tom Brocher, Walter Mooney, and Alan Yong at the U.S. Geological Survey provided critical velocity information. I appreciate Scott Callaghan and Phil Maechling at the Southern California Earthquake Center for their help to install and use their Unified Community Velocity Model software framework to extract velocity profiles from California models. I would also like to thank Bill Stephenson and Morgan Moschetti at the U.S. Geological Survey and Brandon Dugan at the Colorado School of Mines for their thorough reviews that significantly improved this report. This effort was funded by the U.S. Geological Survey Earthquake Hazards Program.

Contents

Figures

Tables

Conversion Factors

International System of Units to U.S. customary units

Multiply	By	To obtain
	Length	
meter (m)	3.281	foot (ft)
kilometer (km)	0.6214	mile (mi)
	Wave Speed	
meter per second (m/s)	3.281	foot per second (ft/s)
kilometer per second (km/s)	3280.84	feet per second (ft/s)
	Density	
kilogram per cubic meter (kg/m^3)	0.06242	pound per cubic foot (lb/ft^3)
	Pressure	
pascal (kg/s^2m)	0.000145	pound-force per square inch (lbf/in^2)

Datum

Horizontal coordinate information is referenced to the North American Datum of 1983 (NAD 83).

Abbreviations

3D	three dimensional
GMM	ground motion model
NCM	National Crustal Model
NCMGF	National Crustal Model geologic framework
NWIS	National Water Information System
USGS	U.S. Geological Survey
V_p	compressional-wave velocity
V_s	shear-wave velocity
WUS	western United States

Calibration of the U.S. Geological Survey National Crustal Model

By Oliver S. Boyd

Abstract

The U.S. Geological Survey National Crustal Model (NCM) is being developed to include spatially varying estimates of site response in seismic hazard assessments. Primary outputs of the NCM are continuous velocity and density profiles from the Earth's surface to the mantle transition zone at 410-kilometer (km) depth for each location on a 1-km grid across the conterminous United States. Datasets used to produce the NCM may have a resolution of better than 1 km near the Earth's surface in some regions, but, with increasing depth, NCM resolution decreases to tens to hundreds of kilometers in the mantle. Basic subsurface information is provided by the NCM geologic framework, thermal model, and petrologic and mineral physics database. In this report, the velocities and densities that can be extracted from the NCM are calibrated through the development of a porosity model based on Biot-Gassmann theory and more than 2,000 compressional- and (or) shear-wave velocity profiles less than 10 km deep from across the conterminous United States and southwestern Canada.

Sediment and rock porosities are derived from shear-wave velocity and are found to depend on effective pressure, rock type, and age (for sedimentary and extrusive volcanic deposits). Porosity-effective pressure functions are then estimated for each rock type (and age for sedimentary and extrusive volcanic deposits). Unconsolidated sediments are found to have higher porosities than consolidated units, which have higher porosities than unweathered igneous units; young sedimentary units (for example, Quaternary age units) tend to have higher porosities than older sedimentary units (for example, pre-Cenozoic age units); porosity decreases with increasing effective pressure; and porosities can decrease quickly through the weathered layer of intrusive rocks.

Comparing two Los Angeles area velocity models and the U.S. Geological Survey Bay Area velocity model with the NCM, the NCM does a better job on average of reproducing observed shear-wave velocities below 1 km per second because it has less bias and uncertainty. Approaching and above 1 km per second, the NCM tends to underpredict observed shear-wave velocity. Whereas several factors could contribute to this, the primary factor is probably bias in the NCM geologic framework. For example, the NCM will predict lower velocities in places where the depth to bedrock and basement appear shallower in the measured velocity profiles than specified in the NCM geologic framework. With regard to observed compressional-wave velocity and density, the NCM has significantly less bias than California models for the former, especially below 2 km per second, and all models tend to overpredict density for densities less than about 2,200 kilograms per cubic meter.

Introduction

Seismic hazards and associated risks are present in many regions across the United States. Large historic earthquakes have occurred along the San Andreas Fault, within the New Madrid seismic zone, in the Puget Lowland, outside of Charleston, South Carolina, and near Washington, D.C. These events, coupled with seismically vulnerable structures built before modern building codes, particularly in the central and eastern United States, lead to appreciable risk from earthquakes. A major factor in assessing seismic hazards is the ground motion produced by an earthquake, which is strongly influenced by the subsurface geology. For example, because of differences in mechanical properties, ground composed of poorly consolidated sediments typically undergoes shaking of greater intensity than ground composed of bedrock such as granite or sandstone. Ground shaking within sedimentary basins may be of greater duration and amplitude relative to locations outside of these basins because of mechanical properties and wave focusing. Knowledge of the surface and subsurface geologic variations can be used to constrain, interpolate, and extrapolate geophysical data and create a model of the three-dimensional (3D) geophysical structure across the United States.

A U.S. Geological Survey (USGS) National Crustal Model (NCM) is being developed to assist with earthquake-hazard estimates in the USGS National Seismic Hazard Model by supporting estimates of ground shaking in response to an earthquake. Improved hazard assessments may also be used for planning and risk assessments but are not intended for site-specific engineering applications. The NCM is composed of geophysical attribute-depth profiles on a 1-kilometer (km) grid from which metrics can be extracted for

ground motion models (GMMs). Because of their application in the western United States (WUS) GMMs, the time-averaged shear-wave velocities in the upper 30 meters (m; termed V_{S30}) and the depths to 1.0 and 2.5 kilometers/second (km/s) shear-wave velocities (termed $Z_{1.0}$ and $Z_{2.5}$) are parameters of immediate interest. The NCM has the flexibility to provide additional metrics such as fundamental frequency, a fully frequency-dependent site-response function derived from one-dimensional, two-dimensional, or 3D analyses, or 3D geophysical volumes for wavefield simulations. The NCM may also benefit other aspects of seismic hazard analysis through better accounting for path-dependent attenuation, path-dependent geometric spreading, and more accurate estimation of earthquake-source properties such as hypocentral location, magnitude, focal mechanism, and stress drop.

Each geophysical profile within the NCM is based on subsurface geology, porosity, effective and total stress, temperature, and mineral- and rock-physics theory. The primary elements used to construct the NCM are: (1) 3D geologic framework (Boyd, 2019), (2) petrologic and mineral physics database (Sowers and Boyd, 2019), (3) 3D temperature model (Boyd, 2020b), (4) calibration of a porosity model for the estimation of bulk rock density and seismic velocity (this report), and (5) validation. These elements make use of a host of geology, borehole, gravity, and seismic datasets to connect subsurface geological variability with geophysical attributes and seismic response.

Seismic velocities within the NCM are determined using Biot-Gassmann theory (Lee, 2010), in which the elastic moduli of geologic units are determined by porosity, saturation, the bulk modulus of air and water, and the elastic moduli of the solid-rock matrix. The NCM seismic velocity profiles are calibrated by estimating how quickly porosity decreases with depth for each geologic unit within the NCM geologic framework (NCMGF) by using measured velocity and density profiles across the United States. The resulting calibration coefficients and supplementary information are available in the associated data release (Boyd, 2020a), and codes to produce geophysical attribute profiles are available at the NCM code repository at https://code.usgs.gov/ghsc/nshmp/ncm/.

Biot-Gassmann Theory

To model the velocity and density of a porous material as a function of depth, Biot-Gassmann theory as presented by Lee (2010) is used in which porosity, ϕ, plays a vital role.

The compressional-wave velocity V_P and shear-wave velocity V_S through a composite material denoted by the subscript b is given by

$$V_P = \sqrt{\frac{k_b + 4\mu_b/3}{\rho_b}} \text{ and} \tag{1}$$

$$V_S = \sqrt{\frac{\mu_b}{\rho_b}}, \tag{2}$$

which are a function of bulk density, ρ_b, and bulk and shear moduli, k_b and μ_b. The density is a linear combination of the density of the solid-rock matrix, denoted in the following by the subscript lowercase s; the density of material within the pore space, denoted by the subscripts w and a for the densities of water and air:

$$\rho_b = \rho_s(1-\phi) + S\rho_w\phi + (1-S)\rho_a\phi, \tag{3}$$

and where S is the fraction of pore space saturated with water.

The bulk and shear moduli are functions of the moduli of the solid-rock matrix, again denoted by the subscript lowercase s; the average bulk modulus, denoted by the subscript av; and the Biot coefficients β_P and β_S; and are given by

$$k_b = k_s(1-\beta_P) + \beta_P^2 k_{av} \text{ and} \tag{4}$$

$$\mu_b = \mu_s(1-\beta_S). \tag{5}$$

The average bulk modulus is determined from the average compressibility given by

$$\frac{1}{k_{av}} = \frac{\beta_P - \phi_N}{k_s} + \frac{\phi_N}{k_{w,a}}, \tag{6}$$

and a Voigt (1928) average, dependent on saturation, is chosen for the effective modulus of the pore space, $k_{w,a}$, which essentially is based on the assumption of patchy saturation (Mavko and Mukerji, 1998). The Biot coefficients are

$$\beta_P = \frac{\phi_N(1+\alpha)}{1+\alpha\phi_N} \text{ and} \tag{7}$$

$$\beta_S = \frac{\phi_N(1+\gamma\alpha)}{1+\gamma\alpha\phi_N}. \tag{8}$$

The average compressibility and Biot coefficients differ from Lee's original presentation in that the porosities are normalized by a maximum porosity

$$\phi_N \equiv \frac{\phi}{\phi_{max}}, \tag{9}$$

which is defined so that at the surface, the maximum porosity, ϕ_{max}, corresponds to the condition where the pressure of water within the pore space is equal to and increases at the same rate as the solid-rock-matrix pressure. This modification accommodates the modeling of very low observed shear-wave velocities (less than 100 m/s). Without this modification, these low velocities would require very high porosities so that pore pressure would be greater and increase faster than the solid-rock-matrix pressure, leading to steadily increasing porosity with depth. Applying a maximum porosity and using

it to normalize the porosity in equations 7 and 8 prevents this condition. At the maximum porosity, the shear modulus of the aggregate material is zero, and the bulk modulus is the average defined by equation 6. Typically, this maximum porosity is about 70 to 80 percent, depending on the density of the minerals that make up the rock matrix.

This maximum porosity, where pore space is saturated with water, is a lower bound. If saturated with air, the maximum porosity would be closer to 1, and a transition between the two would depend on the depth to the water table and saturation. For simplicity, the lower value of maximum porosity is chosen.

The parameters γ and α in the Biot coefficients, where the latter is referred to as the consolidation parameter, control the Biot coefficients' sensitivity to pressure. The former, γ, is also a function of α and is given by

$$\gamma = \frac{(1+m\alpha)}{1+\alpha}, \tag{10}$$

where m and α account for differential pressure, ΔP, which represents the rock's vertical stress minus its pore pressure. These parameters, with ΔP given in megaPascals, are specified by

$$m = M_1 \Delta P^{M_E} \text{ and} \tag{11}$$

$$\alpha = A_1 \Delta P^{A_E}, \tag{12}$$

where α is not allowed to rise above a constant A_2, and m is not allowed to fall below another constant M_2. Several of these constants differ from those presented in Lee (2010) because of the use of normalized porosity in equations 6 through 8. Simultaneous grid-search fitting of the porosity, compressional-wave velocity, and shear-wave velocity in saturated sands near the Gulf of Mexico from Zimmer (2003), which was used in the analysis of Lee (2010), yields constants M_1, A_1, and A_2 equal to 10, 30, and 11, respectively. The constant M_2 equal to 2, and exponents M_E equal to −0.6 and A_E equal to −0.4, were retained from Lee (2010). From a chi-squared analysis of residuals, M_1, M_E, and A_2 are found to have natural log ($\log_e$) standard deviations of 0.16, 0.21, and 0.14, respectively. The parameters M_2, A_E, and A_1 have nearly one-sided chi-squared distributions so that these parameters are likely to be less than 3.4, greater than 21, and greater than −0.55 (mean plus or minus one standard deviation in $\log_e$ space), respectively. These values were determined for saturated sands, and how they may vary according to lithology is unknown. The resulting NCM shear-wave velocity model, however, will not depend on the choice of constants because observed shear-wave velocities are used to derive lithology-dependent porosity-depth relations, which are then used to calculate the shear-wave velocities in the model. NCM bulk density and compressional-wave velocities will, however, be sensitive to variations in these constants and the resulting porosity relations.

A functional form for porosity is assumed in which porosity cannot be equal to or less than 0 nor equal to or greater than 1, and the differential pressure normalized by surface pressure is not equal to or less than 0. These assumptions result in the following equation:

$$log(-log(\phi)) = Alog(\Delta P_N)^{0.5} + B, \tag{13}$$

where the constants A and B are functions of rock type and age (explained further in the "Subsurface Porosity" section). The exponent 0.5 in this equation was chosen after visual inspection of the estimates of porosity versus pressure that are shown in the "Results" section. Although conceivably this exponent also depends on rock type and age, for simplicity and to guard against overfitting limited data, no attempt was made to include this dependence.

Subsurface Porosity

Equations 2, 3, 5, 8, 10, 11, and 12 are combined and rearranged to solve for porosity as a function of shear-wave velocity, differential pressure, and shear modulus and density of the solid-rock matrix and pore-space material. Moduli and density of the solid-rock matrix are estimated by applying mineral physics information from the NCM Petrologic and Mineral Physics Database (Sowers and Boyd, 2019) to geologic profiles from the NCMGF (Boyd, 2019) that are adjusted by eye at each measurement location. Calibration proceeds by estimating A and B in equation 13 by using a robust linear least-squares regression for each rock type and age within the NCMGF and separately at each measurement location. The latter is done to allow for the spatial variability of B for a given lithology. The coefficients A and B are further refined to ensure that the resulting porosity-pressure relationships reproduce the observed shear-wave velocities.

A more direct approach would be to estimate porosity as a function of bulk density (by rearranging the variables in eq. 3); however, the quantity of primary interest for seismic hazard studies is shear-wave velocity. Developing a porosity model derived from shear-wave velocities will ensure that when that model is applied, shear-wave velocities will be estimated with minimal bias. Although measurements of shallow-depth density are few and no collocated density and shear-wave-velocity measurements have been made, additional analysis is warranted.

Measured Velocities and Densities

Seismic velocity and density profiles and V_{S30} values at 6,791 distinct locations across the United States were gathered from several existing studies (table 1; fig. 1), and

modest improvements and simplifications were made. For example, the database compiled by Ahdi and others (2017) is composed solely of shear-wave-velocity profiles reported to depths of 70 m, but many of the underlying studies included shear-wave-velocity profiles that extend to depths of several thousand meters as well as compressional-wave velocities. This additional information is included here. Regarding simplification, if profiles are specified as a series of constant-velocity layers, the velocity is assigned as a single value to the middle of the layer.

Shallow to moderately deep (0–10 km depth) shear-wave-velocity profiles were used to calculate and calibrate the porosity model, whereas measured compressional-wave velocities were compared with predicted velocities to better understand how well the underlying Biot-Gassmann theory is working and under what conditions it should be modified. Improvements to analyses may be gained by using the following: the USGS V_{S30} database (Yong and others, 2016); velocity profiles from Mooney (2013), which tend to have few samples in the upper few kilometers but extend deep into the mantle; and density profiles. In all, nearly 30,000 shear-wave-velocity observations extending from the surface to a depth of almost 10 km (fig. 2) were used for calibration.

Subsurface Geology

Lithologic profiles, which include multiple rock units of varying age and petrology, were used to calculate the solid-rock-matrix moduli and density (subscript lowercase *s* in eqs. 3, 4, and 5) as well as to estimate the values of the constants *A* and *B*, which depend on rock type and age, in the porosity function (eq. 13). These profiles were extracted from the NCMGF at each shear-wave velocity-measurement location. The mineralogy for each rock type and the methods used to calculate mineral moduli and density are specified in the NCM petrologic and mineral physics database (Sowers and Boyd, 2019). The depths of geologic contacts within these profiles are iteratively adjusted to reflect observed velocity variations and refined lithology-dependent *A* and *B* values. In some cases, the lithology and geologic contacts that are noted in geologic logs (see for example, Gibbs and others [1992]) can be correlated with mapped surface geology and contacts within the NCMGF. Although these geologic logs were considered, contacts were typically inferred from changes in seismic velocity and similarity to inferred lithology-dependent, porosity-effective pressure relationships.

This effort yields obvious problems with the NCMGF as noted in its associated documentation. One limitation of the NCMGF is that units that are not present at the surface cannot be propagated into the subsurface. This is seen, for example, in the Georgia Basin at the border of Washington and British Columbia, where the Miocene to Pliocene Boundary Bay Formation, which consists primarily of sandstone and mudstone (Mustard and Rouse, 1994), underlies unconsolidated Quaternary sediments. The Boundary Bay Formation is not present in the geologic map compilation of Garrity and Soller (2009). In this case, Miocene sandstone has been inserted into an updated version of the NCMGF in this region. In another example from the valleys near Salt Lake City, Utah, semiconsolidated glaciolacustrine deposits beneath unconsolidated sediment and mud (Stephenson and others, 2012) are missing from the NCMGF in much of the region because of very few nearby outcrops. Here, a late Pliocene medium-grained, mixed-clastic rock, as observed in these nearby outcrops, has been inserted into an updated version of the NCMGF.

Table 1. Seismic velocity and density datasets collected across the United States.

[V_P, compressional-wave velocity; V_S, shear-wave velocity; ρ, density; V_{S30}, time-averaged shear-wave velocity to 30-meters depth]

Dataset	Region	Number of profiles	Type
Boore (2003)	California, Oregon, and Washington	277	V_P, V_S
Shi and Asimaki (2018)	California, Oregon, and Washington	176	V_S
Brocher and others (1998), Brocher (2005a)	California	114	V_P, ρ
Brocher and Horta (1998)	Oregon	9	V_P, ρ
Brocher and Ruebel (1998)	Washington	22	V_P, ρ
Ahdi and others (2017)	California, Oregon, Washington, and southwestern Canada	996	V_P, V_S
Kohler and others (2003)	Los Angeles, California	367	V_P, V_S
Magistrale and others (2008)	Wasatch Front, Utah	229	V_P, V_S
Kansas Geological Survey (2017)	Kansas	117	V_P, ρ
Hashash and others (2014)	Central and eastern United States	58	V_P, V_S
Yong and others (2016)	Conterminous United States	2,763	V_{S30}
Mooney (2013)	North America east of longitude 115°W	2,603	V_P, V_S

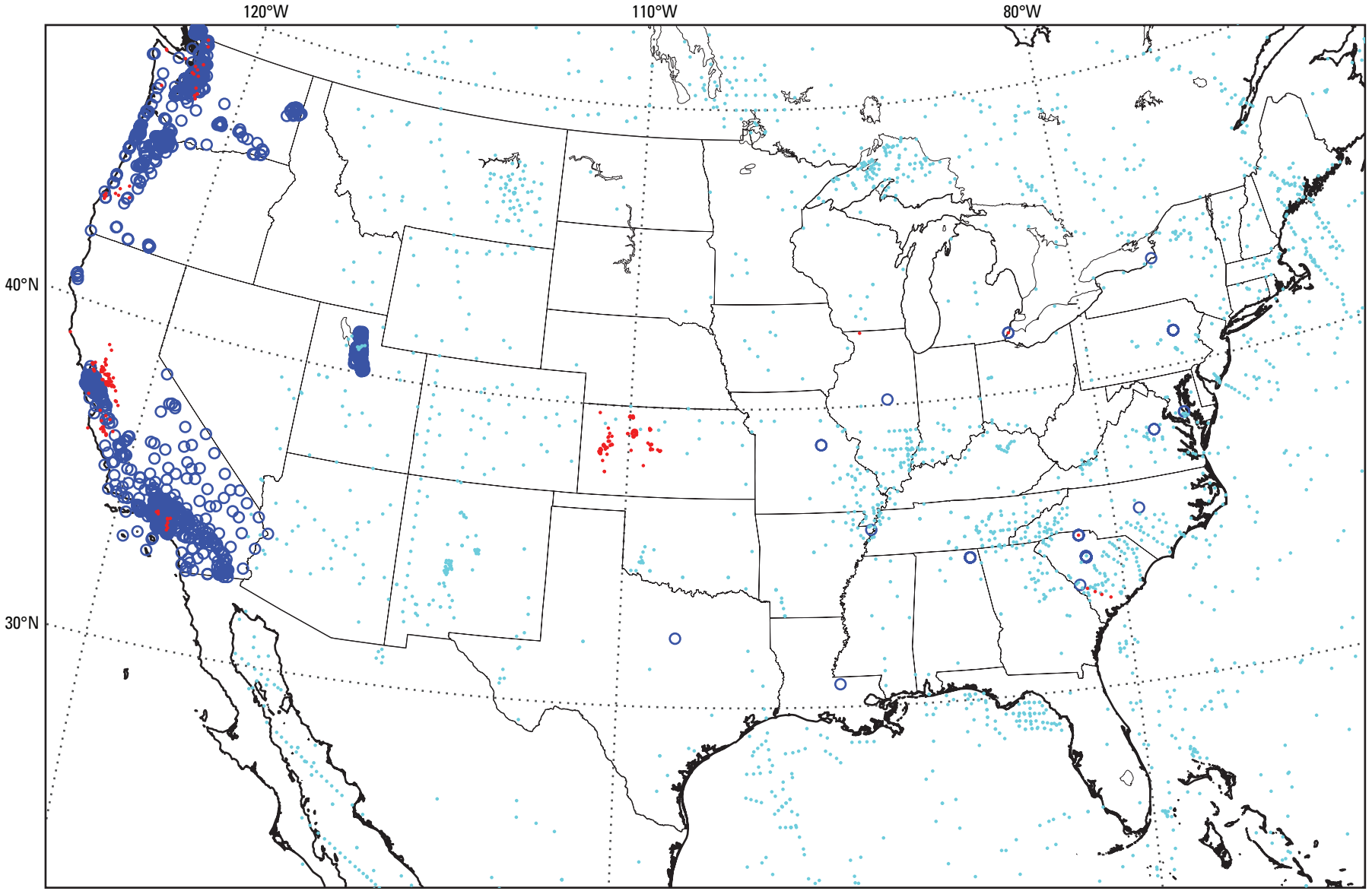

Figure 1. Locations of geophysical profiles collected within the domain of the National Crustal Model. Blue circles are shear-wave and, in some cases, compressional-wave velocity profiles; red dots are compressional-wave velocity and density profiles; and cyan dots are deep (tens to hundreds of kilometers; modified from Mooney, 2013) shear-wave and compressional-wave-velocity profiles.

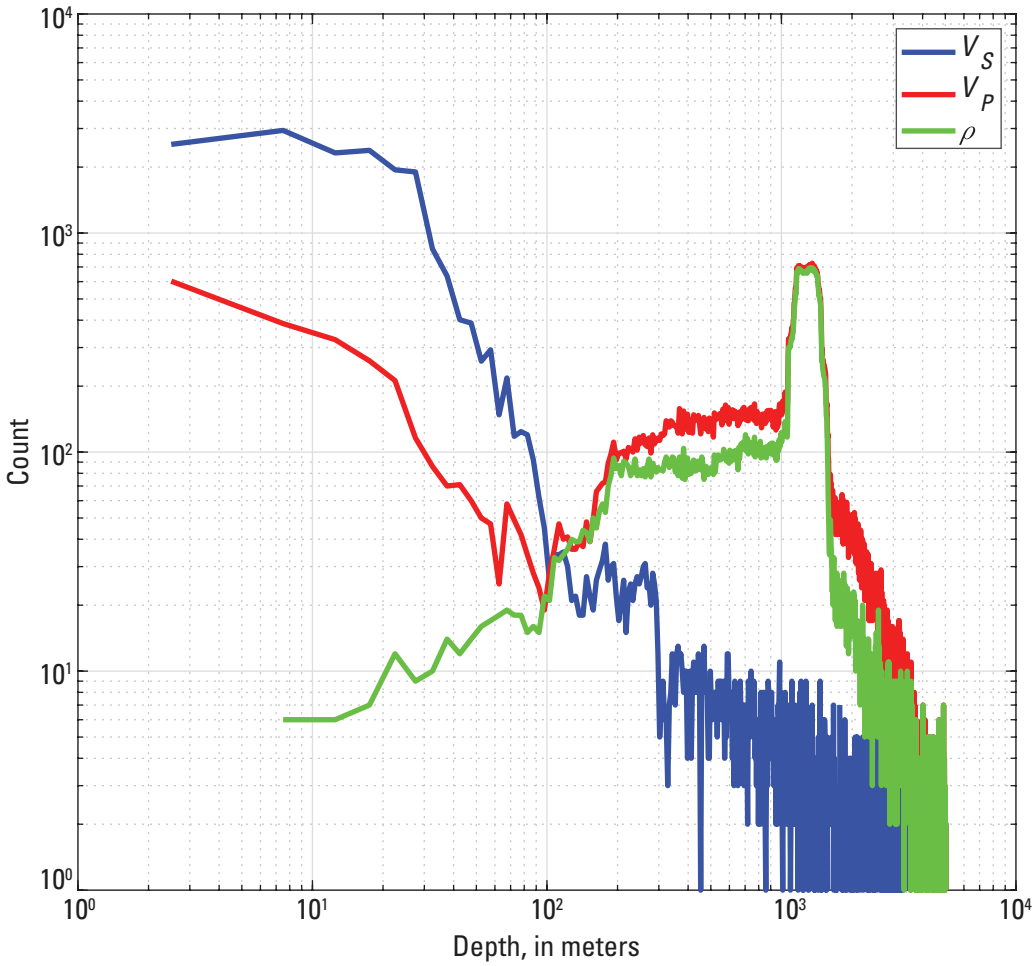

Figure 2. Histograms of depths at which densities and compressional-wave and shear-wave velocities are measured, not including Mooney's (2013) compilation. Histogram bin widths are 5 meters depth. (V_S, shear-wave velocity; V_P, compressional-wave velocity; ρ, density)

Results

A total of 162 unique lithology-age combinations from 57 rock types are available for analysis (table 2 and 3). Rock types from granite and basalt to sandstone and limestone to unconsolidated sediment span ages from Proterozoic to Holocene. Examples for three rock types showing porosity versus differential pressure normalized by surface pressure and shear-wave velocity versus depth are shown in figure 3.

As expected, porosity decreases with increasing differential pressure or depth and is greatest for unconsolidated rock types. Lithified sedimentary units have a large range in porosity from nearly 0 to almost 40 percent at 100-m depth, and intrusive igneous units generally have moderate porosity that decreases quickly with depth to less than 5 percent below the weathered zone, which is, in most cases, less than 100 m thick. When separated by rock type and age, large ranges in A and B (eq. 13) result. For simplicity, a single average slope, A, is estimated for each rock type, and in the first iteration, the intercept, B, is estimated independently for each rock type and age. Intercepts for sedimentary and extrusive volcanic rock types are found to increase with age (because porosities decrease) as shown in figure 4 according to

$$B = CAge^{0.25} + D, \tag{14}$$

where Age is in millions of years, and D is a constant dependent on rock type. The exponent 0.25 is subjectively chosen from visual inspection to linearize estimates of B versus Age. The constant C has been found to be 0.29 ± 0.12, which is used for rock indexes 1 through 115. A single average value of B is used for intrusive and metamorphic rock types, which have indexes 116 through 209. Values for A, B, and D along with their uncertainties are given in table 2 and 3.

Several rock types are not represented, or their porosities have been estimated only once or twice on the basis of few observations. In these cases, their slopes are assigned on the

Table 2. Constants *A* and *D* for sedimentary and extrusive rocks (indexes 1 to 115) along with their standard deviations for equations 13 and 14, which are needed to calculate porosity and geophysical attributes for each geologic unit. The columns N V_S Obs and N V_S Prof provide the total number of data points and profiles, respectively, in which each unit appears. Blank cells indicate that the rock type did not have data with which to estimate uncertainty. Please see the ScienceBase data release associated with this report (Boyd, 2020a) for an accessible version of the most up-to-date coefficients.

[*A*, slope relating porosity and pressure in equation 13; σ_A, standard deviation of *A*; *D*, intercept in equation 14; σ_D, standard deviation of *D*]

Index	Rock type	N V_S Obs	N V_S Prof	*A* (unitless)	σ_A	*D* (unitless)	σ_D
1	Unconsolidated material	6,299	347	0.44	0.006	−0.98	0.008
2	Alluvium	1,656	358	0.54	0.018	−0.89	0.018
3	Silt	106	11	0.43	0.045	−1.07	0.043
4	Sand	231	44	0.49	0.029	−1.12	0.029
5	Floodplain	0	0	0.54		−0.89	
6	Gravel	73	12	0.63	0.097	−0.45	0.112
7	Levee	0	0	0.44		−0.98	
8	Delta	0	0	0.54		−0.89	
9	Alluvial fan	0	0	0.54		−0.89	
10	Alluvial terrace	0	0	0.54		−0.89	
11	Lake or marine sediment	646	99	0.48	0.019	−1.17	0.020
12	Playa	0	0	0.48		−1.17	
13	Mud flat	0	0	0.48		−1.17	
14	Beach sand	0	0	0.49		−1.12	
15	Terrace	0	0	0.49		−1.12	
16	Eolian	0	0	0.49		−1.12	
17	Dune sand	0	0	0.49		−1.12	
18	Sand sheet	0	0	0.49		−1.12	
19	Loess	0	0	0.49		−1.12	
20	Volcanic ash	0	0	0.49		−1.12	
21	Mass-wasting material	0	0	0.63		−0.45	
22	Colluvium	0	0	0.63		−0.45	
23	Mudflow	0	0	0.46		−1.01	
24	Lahar	0	0	0.63		−0.45	
25	Debris flow	0	0	0.63		−0.45	
26	Landslide	0	0	0.63		−0.45	
27	Talus	0	0	0.63		−0.45	
28	Glacial drift	1,407	194	0.44	0.014	−0.60	0.020
29	Till	11	2	0.83	0.150	–0.79	0.222
30	Moraine	0	0	0.44		−0.60	
31	Stratified glacial sediment	0	0	0.44		−0.60	
32	Glacial outwash sediment	0	0	0.44		−0.60	
33	Outwash	0	0	0.44		−0.60	
34	Sub-/supra-glacial sediment	0	0	0.44		−0.60	
35	Glaciolacustrine	0	0	0.44		−0.60	
36	Glacial-marine sediment	0	0	0.46		−0.06	

Table 2. Constants *A* and *D* for sedimentary and extrusive rocks (indexes 1 to 115) along with their standard deviations for equations 13 and 14, which are needed to calculate porosity and geophysical attributes for each geologic unit. The columns N V_S Obs and N V_S Prof provide the total number of data points and profiles, respectively, in which each unit appears. Blank cells indicate that the rock type did not have data with which to estimate uncertainty. Please see the ScienceBase data release associated with this report (Boyd, 2020a) for an accessible version of the most up-to-date coefficients.—Continued

[*A*, slope relating porosity and pressure in equation 13; σ_A, standard deviation of *A*; *D*, intercept in equation 14; σ_D, standard deviation of *D*]

Index	Rock type	N V_S Obs	N V_S Prof	*A* (unitless)	σ_A	*D* (unitless)	σ_D
37	Biogenic material	0	0	0.37		−0.72	
38	Peat	9	1	0.37	0.157	−0.72	0.107
39	Coral	0	0	0.70		−0.39	
40	Residuum	402	23	2.05	0.154	−2.76	0.166
41	Clay or mud	2,860	215	0.46	0.008	−1.01	0.010
42	Sedimentary rock	0	0	0.43		−0.69	
43	Clastic rock	0	0	0.42		−0.48	
44	Mudstone	133	42	0.49	0.066	−0.94	0.076
45	Claystone	12	1	0.39	1.279	−0.78	3.316
46	Bentonite	0	0	0.39		−0.78	
47	Shale	84	9	0.39	0.042	−0.64	0.053
48	Black shale	62	8	0.39	0.116	−0.91	0.140
49	Oil shale	0	0	0.39		−0.91	
50	Argillite	130	20	0.62	0.066	−1.25	0.083
51	Siltstone	118	33	0.45	0.072	−0.63	0.080
52	Fine-grained mixed clastic rock	0	0	0.42		−0.48	
53	Sandstone	3,862	706	0.49	0.007	−0.91	0.010
54	Arenite	0	0	0.49		−0.91	
55	Orthoquartzite	22	2	0.37	0.098	−0.88	0.110
56	Calcarenite	0	0	0.70		−0.39	
57	Arkose	238	30	0.25	0.057	−0.34	0.068
58	Wacke	0	0	0.29		−0.47	
59	Graywacke	94	10	0.29	0.076	−0.47	0.093
60	Medium-grained mixed clastic rock	708	116	0.42	0.032	−0.48	0.036
61	Conglomerate	482	79	0.69	0.050	−1.07	0.117
62	Sedimentary breccia	5	1	0.42	0.336	−0.81	0.360
63	Coarse-grained mixed clastic rock	0	0	0.42		−0.48	
64	Olistostrome	0	0	0.49		−0.94	
65	Melange	27	6	0.57	0.194	−0.65	0.211
66	Carbonate rock	0	0	0.70		−0.39	
67	Limestone	1,201	22	0.70	0.061	−0.39	0.092
68	Dolostone	366	4	0.01	0.065	0.10	0.117
69	Mixed carbonate/clastic rock	0	0	0.56		0.01	
70	Mixed volcanic/clastic rock	0	0	0.49		−0.24	
71	Phosphorite	0	0	0.43		−0.69	
72	Chemical sedimentary rock	0	0	0.43		−0.69	

Table 2. Constants *A* and *D* for sedimentary and extrusive rocks (indexes 1 to 115) along with their standard deviations for equations 13 and 14, which are needed to calculate porosity and geophysical attributes for each geologic unit. The columns N V_S Obs and N V_S Prof provide the total number of data points and profiles, respectively, in which each unit appears. Blank cells indicate that the rock type did not have data with which to estimate uncertainty. Please see the ScienceBase data release associated with this report (Boyd, 2020a) for an accessible version of the most up-to-date coefficients.—Continued

[*A*, slope relating porosity and pressure in equation 13; σ_A, standard deviation of *A*; *D*, intercept in equation 14; σ_D, standard deviation of *D*]

Index	Rock type	N V_S Obs	N V_S Prof	*A* (unitless)	σ_A	*D* (unitless)	σ_D
73	Evaporite	0	0	0.43		−0.69	
74	Chert	0	0	0.43		−0.69	
75	Novaculite	0	0	0.43		−0.69	
76	Iron formation	0	0	0.43		−0.69	
77	Exhalite	0	0	0.43		−0.69	
78	Coal	0	0	0.43		−0.69	
79	Mixed coal/clastic rock	0	0	0.43		−0.69	
80	Volcanic rock	0	0	0.56		−0.90	
81	Glassy volcanic rock	0	0	0.56		−0.90	
82	Obsidian	0	0	0.56		−0.90	
83	Vitrophyre	0	0	0.56		−0.90	
84	Pumice	0	0	0.56		−0.90	
85	Pyroclastic rock	0	0	0.56		−0.90	
86	Tuff	0	0	0.56		−0.90	
87	Welded tuff	0	0	0.56		−0.90	
88	Ash-flow tuff	0	0	0.56		−0.90	
89	Ignimbrite	0	0	0.56		−0.90	
90	Volcanic breccia	0	0	0.56		−0.90	
91	Lava flow	0	0	0.56		−0.90	
92	Bimodal suite	0	0	0.56		−0.90	
93	Felsic volcanic rock	12	2	0.57	0.262	−0.53	0.203
94	Alkali-feldspar rhyolite	0	0	0.57		−0.76	
95	Rhyolite	72	14	0.57	0.102	−0.76	0.099
96	Rhyodacite	0	0	0.57		−0.76	
97	Dacite	0	0	0.57		−0.76	
98	Alkali-feldspar trachyte	0	0	0.48		−0.84	
99	Trachyte	0	0	0.48		−0.84	
100	Quartz latite	0	0	0.48		−0.84	
101	Latite	33	9	0.48	0.082	−0.84	0.101
102	Intermediate volcanic rock	62	18	0.48	1.322	−1.03	3.359
103	Trachyandesite	0	0	0.43		−0.73	
104	Andesite	187	24	0.43	0.064	−0.73	0.079
105	Mafic rock	45	5	0.68	0.105	−1.05	0.124
106	Trachybasalt	0	0	0.68		−1.34	
107	Basalt	670	94	0.68	0.036	−1.34	0.040
108	Tholeiite	0	0	0.68		−1.34	

Table 2. Constants *A* and *D* for sedimentary and extrusive rocks (indexes 1 to 115) along with their standard deviations for equations 13 and 14, which are needed to calculate porosity and geophysical attributes for each geologic unit. The columns N V_S Obs and N V_S Prof provide the total number of data points and profiles, respectively, in which each unit appears. Blank cells indicate that the rock type did not have data with which to estimate uncertainty. Please see the ScienceBase data release associated with this report (Boyd, 2020a) for an accessible version of the most up-to-date coefficients.—Continued

[*A*, slope relating porosity and pressure in equation 13; σ_A, standard deviation of *A*; *D*, intercept in equation 14; σ_D, standard deviation of *D*]

Index	Rock type	N V_S Obs	N V_S Prof	*A* (unitless)	σ_A	*D* (unitless)	σ_D
109	Hawaiite	0	0	0.68		−1.34	
110	Alkaline basalt	0	0	0.68		−1.34	
111	Alkalic volcanic rock	0	0	0.68		−1.34	
112	Phonolite	0	0	0.68		−1.34	
113	Tephrite	0	0	0.68		−1.34	
114	Ultramafitite	0	0	0.68		−1.34	
115	Volcanic carbonatite	0	0	0.68		−1.34	

Table 3. Constants *A* and *B* for intrusive and metamorphic rocks (indexes 116 to 209) along with their standard deviations for equation 13, which is needed to calculate porosity and geophysical attributes for each geologic unit. The columns N V_S Obs and N V_S Prof provide the total number of data points and profiles, respectively, in which each unit appears. Blank cells indicate that the rock type did not have data with which to estimate uncertainty. Please see the ScienceBase data release associated with this report (Boyd, 2020a) for an accessible version of the most up-to-date coefficients.

[*A*, slope relating porosity and pressure in equation 13; σ_A, standard deviation of *A*; *B*, intercept in equation 14; σ_B, standard deviation of *B*]

Index	Rock type	N V_S Obs	N V_S Prof	*A* (unitless)	σ_A	*B* (unitless)	σ_B
116	Plutonic rock	0	0	0.74		0.00	
117	Aplite	0	0	0.87		0.06	
118	Porphyry	0	0	0.87		0.06	
119	Lamprophyre	0	0	0.87		0.06	
120	Pegmatite	0	0	0.87		0.06	
121	Granitoid	40	9	0.87	0.154	0.06	0.166
122	Charnockite	0	0	0.87		0.06	
123	Alkali-feldspar granite	0	0	0.87		0.06	
124	Quartz monzodiorite	0	0	0.87		−0.32	
125	Monzodiorite	0	0	0.87		−0.32	
126	Quartz diorite	9	2	0.87	0.401	−0.32	0.426
127	Diorite	3	1	0.87	0.599	−0.20	0.764
128	Diabase	0	0	0.77		−0.27	
129	Granite	139	34	0.77	0.096	−0.27	0.110
130	Peraluminous granite	0	0	0.77		−0.27	
131	Metaluminous granite	0	0	0.77		−0.27	
132	Subaluminous granite	0	0	0.77		−0.27	
133	Peralkaline granite	0	0	0.77		−0.27	
134	Granodiorite	378	77	0.87	0.060	−0.19	0.067
135	Tonalite	50	10	1.01	0.141	−0.29	0.162
136	Trondhjemite	0	0	1.01		−0.29	
137	Alkali-feldspar syenite	0	0	0.77		−0.27	

Table 3. Constants *A* and *B* for intrusive and metamorphic rocks (indexes 116 to 209) along with their standard deviations for equation 13, which is needed to calculate porosity and geophysical attributes for each geologic unit. The columns N V_S Obs and N V_S Prof provide the total number of data points and profiles, respectively, in which each unit appears. Blank cells indicate that the rock type did not have data with which to estimate uncertainty. Please see the ScienceBase data release associated with this report (Boyd, 2020a) for an accessible version of the most up-to-date coefficients.—Continued

[*A*, slope relating porosity and pressure in equation 13; σ_A, standard deviation of *A*; *B*, intercept in equation 14; σ_B, standard deviation of *B*]

Index	Rock type	N V_S Obs	N V_S Prof	*A* (unitless)	σ_A	*B* (unitless)	σ_B
138	Quartz syenite	0	0	0.77		−0.27	
139	Syenite	0	0	0.77		−0.27	
140	Quartz monzonite	56	9	0.47	0.168	0.48	0.197
141	Monzonite	0	0	0.47		0.48	
142	Gabbroid	0	0	0.47		0.20	
143	Quartz monzogabbro	0	0	0.47		0.20	
144	Monzogabbro	0	0	0.47		0.20	
145	Quartz gabbro	0	0	0.47		0.20	
146	Gabbro	4	2	0.47	0.451	0.20	0.478
147	Norite	0	0	0.47		0.20	
148	Troctolite	0	0	0.47		0.20	
149	Anorthosite	0	0	0.47		0.20	
150	Alkalic intrusive rock	0	0	0.47		0.20	
151	Nepheline syenite	0	0	0.47		0.20	
152	Ultramafic intrusive rock	11	1	0.47	0.248	0.53	0.268
153	Peridotite	0	0	0.47		0.53	
154	Dunite	0	0	0.47		0.53	
155	Kimberlite	0	0	0.47		0.53	
156	Pyroxenite	0	0	0.47		0.53	
157	Hornblendite	0	0	0.47		0.53	
158	Intrusive carbonatite	0	0	0.47		0.53	
159	Metamorphic rock	0	0	0.56		0.38	
160	Hornfels	0	0	0.43		0.44	
161	Eclogite	0	0	0.43		0.44	
162	Greisen	0	0	0.43		0.44	
163	Skarn	0	0	0.43		0.44	
164	Calc-silicate rock	0	0	0.43		0.44	
165	Serpentinite	62	18	0.43	0.100	0.44	0.115
166	Metasedimentary rock	69	18	0.61	0.126	0.23	0.163
167	Meta-argillite	0	0	0.56		0.38	
168	Slate	0	0	0.56		0.38	
169	Quartzite	0	0	0.56		0.38	
170	Metaconglomerate	0	0	0.56		0.38	
171	Marble	0	0	0.56		0.38	
172	Metavolcanic rock	64	6	0.13	0.177	1.61	0.189
173	Felsic metavolcanic rock	1,556	18	0.02	0.016	1.50	0.029
174	Metarhyolite	0	0	0.02		1.50	
175	Keratophyre	0	0	0.48		0.09	
176	Intermediate metavolcanic rock	0	1	0.48		0.09	
177	Mafic metavolcanic rock	0	0	0.47		0.20	

Table 3. Constants *A* and *B* for intrusive and metamorphic rocks (indexes 116 to 209) along with their standard deviations for equation 13, which is needed to calculate porosity and geophysical attributes for each geologic unit. The columns N V_S Obs and N V_S Prof provide the total number of data points and profiles, respectively, in which each unit appears. Blank cells indicate that the rock type did not have data with which to estimate uncertainty. Please see the ScienceBase data release associated with this report (Boyd, 2020a) for an accessible version of the most up-to-date coefficients.—Continued

[*A*, slope relating porosity and pressure in equation 13; σ_A, standard deviation of *A*; *B*, intercept in equation 14; σ_B, standard deviation of *B*]

Index	Rock type	N V_S Obs	N V_S Prof	*A* (unitless)	σ_A	*B* (unitless)	σ_B
178	Metabasalt	0	0	0.68		−0.22	
179	Spilite	0	0	0.68		−0.22	
180	Greenstone	19	4	0.59	0.355	−0.15	0.368
181	Phyllite	3	3	0.59	1.816	0.52	2.152
182	Schist	47	14	0.59	0.107	0.48	0.121
183	Greenschist	0	0	0.59		0.48	
184	Blueschist	0	0	0.59		0.48	
185	Mica schist	216	56	0.38	0.049	−0.02	0.058
186	Biotite schist	0	0	0.38		−0.02	
187	Pelitic schist	7	1	1.35	0.187	−0.78	0.211
188	Quartz-feldspar schist	0	0	1.35		−0.78	
189	Calc-silicate schist	0	0	1.35		−0.78	
190	Amphibole schist	0	0	1.35		−0.78	
191	Granofels	0	0	0.56		0.38	
192	Gneiss	55	9	0.70	0.114	−0.17	0.124
193	Felsic gneiss	0	0	0.70		−0.17	
194	Granitic gneiss	0	0	0.70		−0.17	
195	Biotite gneiss	0	0	0.70		−0.17	
196	Mafic gneiss	0	0	0.70		−0.17	
197	Orthogneiss	57	14	1.05	0.147	−0.37	0.162
198	Paragneiss	0	0	0.38		−0.02	
199	Migmatite	0	0	0.56		0.38	
200	Amphibolite	96	2	0.26	0.082	1.33	0.122
201	Granulite	0	0	0.26		1.33	
202	Tectonite	0	0	0.26		1.33	
203	Tectonic melange	0	0	0.26		1.33	
204	Tectonic breccia	0	0	0.26		1.33	
205	Cataclasite	0	0	0.26		1.33	
206	Phyllonite	0	0	0.26		1.33	
207	Mylonite	0	0	0.26		1.33	
208	Flaser gneiss	0	0	0.70		−0.17	
209	Augen gneiss	0	0	0.70		−0.17	

Figure 3 (following page). Plots of porosity versus normalized differential pressure—vertical stress minus pore pressure divided by surface pressure—(left) and shear-wave velocity versus depth (right) for sand (top), sandstone (middle), and granodiorite (bottom). Different colors correspond to different ages and represent non-overlapping binned mean values. Black dots are individual data points for that geologic unit, and gray dots represent all available data. Lines are fits assuming a single average slope and *B* value that follows equation 14; and the dashed line at the top is the porosity-pressure limit imposed for any given profile. For clarity, note that only 2 of the 19 available sandstone ages are shown. (m, meter; m/s, meter per second)

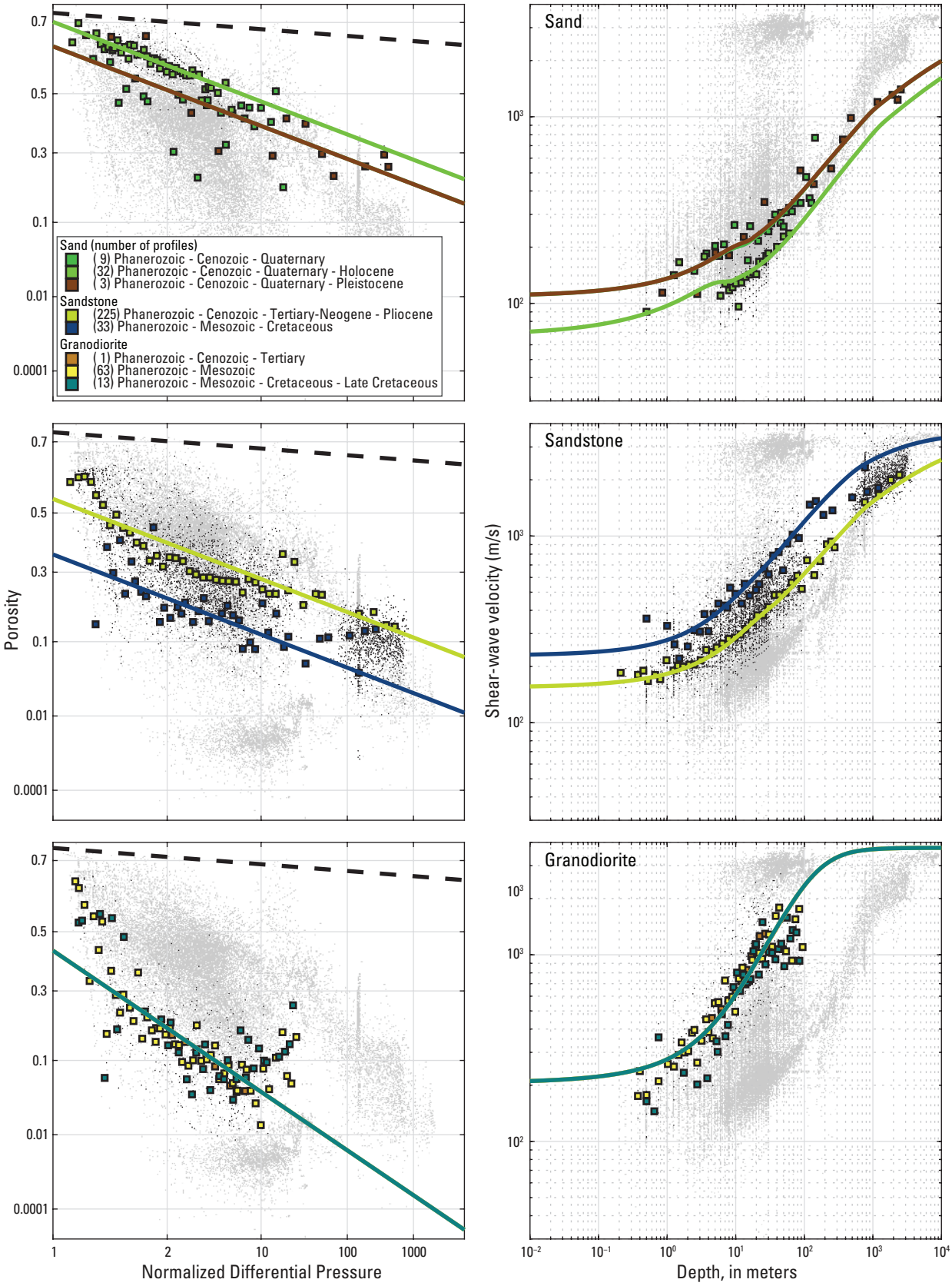
Sand (number of profiles)
(9) Phanerozoic - Cenozoic - Quaternary
(32) Phanerozoic - Cenozoic - Quaternary - Holocene
(3) Phanerozoic - Cenozoic - Quaternary - Pleistocene
Sandstone
(225) Phanerozoic - Cenozoic - Tertiary-Neogene - Pliocene
(33) Phanerozoic - Mesozoic - Cretaceous
Granodiorite
(1) Phanerozoic - Cenozoic - Tertiary
(63) Phanerozoic - Mesozoic
(13) Phanerozoic - Mesozoic - Cretaceous - Late Cretaceous
Sand
Sandstone
Granodiorite
Porosity
Shear-wave velocity (m/s)
Normalized Differential Pressure
Depth, in meters

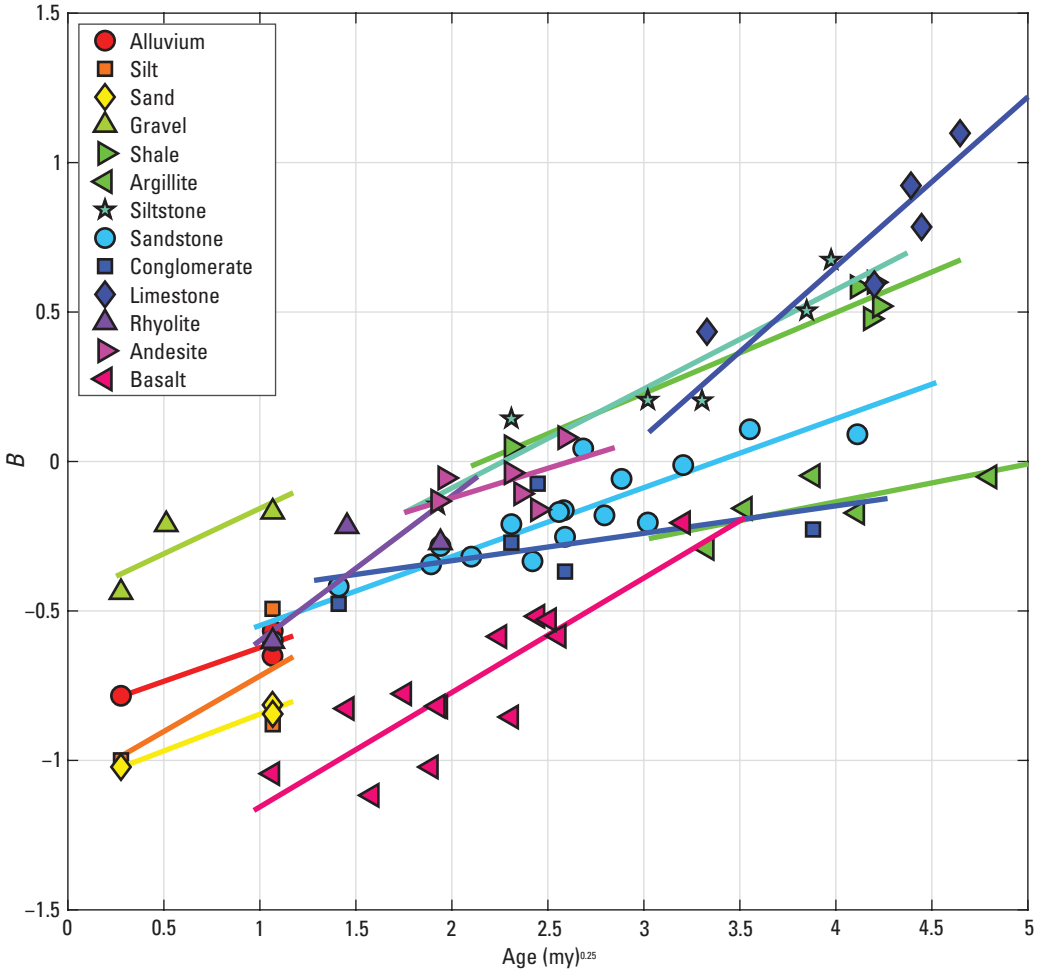

Figure 4. Age versus estimates of *B* for sedimentary and extrusive volcanic rock types. (my, million years)

basis of materials with similar compositions. For more general rock types such as sedimentary and plutonic, which are not explicitly represented in the calibration dataset, averages of the sedimentary and plutonic rock types, respectively, are used.

Whereas decreasing porosity with depth in unconsolidated and sedimentary units can be considered partially the result of compaction during sedimentation, much of the porosity in shallow igneous rocks is due to weathering. As a result, predicting near-surface velocities is problematic if the thickness of this weathering layer is unknown. Pelletier and others (2016) have produced a model of the global surface at 1-km resolution depicting the thickness of weathered rock, but it has not yet been implemented in the NCMGF.

Comparisons with Observed Velocities

Sites having observations of both shear-wave and compressional-wave velocities are used to assess the underlying Biot-Gassmann theory. In figure 5, predictions of shear-wave and compressional-wave velocities based on the adjusted geologic profiles and spatially varying *B* values are shown relative to observations. Whereas the scatterplots do not indicate an apparent bias with depth, the histograms reveal that the underlying Biot-Gassmann theory could use some minor modifications, particularly with respect to the parameters β_P (eq. 7) and γ (eq. 10), in order to better match observations.

Lee (2005) suggested that above the water table, when saturation is less than 100 percent, γ should be equal to 1. This condition on γ causes a significant and sudden jump (more than 200 m/s) in the calculated shear-wave velocity above the water table that is rarely observed in the velocity profiles. Alternatively, γ could be defined as a function of saturation, decreasing to 1 at zero saturation; but here, too, a substantial increase in shear-wave velocity is produced that is not generally observed. In most cases, the shear-wave velocity continues to decrease above the water table, consistent with no change to how γ is formulated. Therefore, equation 10 is maintained above the water table.

The other modification is made to the β_P function. In the standard formulation of this function (eq. 7), compressional-wave velocities above the water table tend to be overestimated (note the asymmetry in the blue curve of the

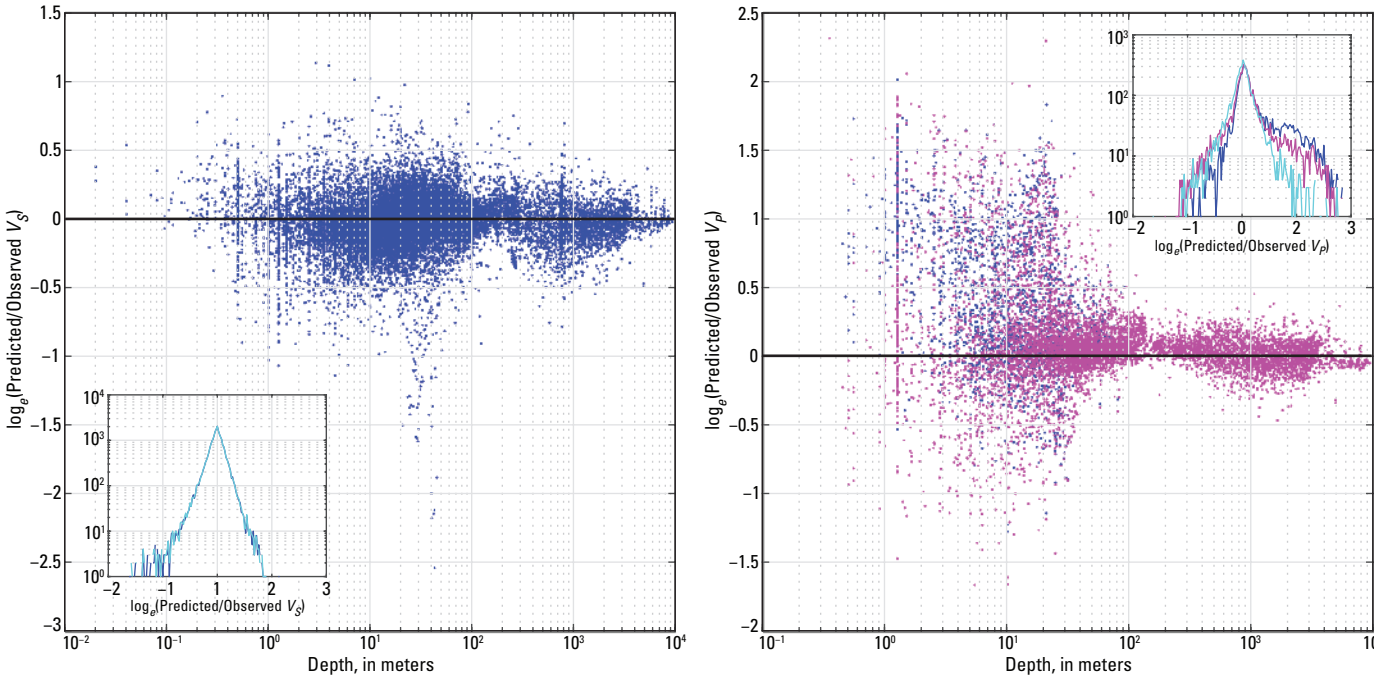

Figure 5. Ratio of predicted relative to observed shear-wave velocity (V_S; left) and compressional-wave velocity (V_P; right) versus depth by using adjusted geologic profiles with spatially varying B values. In the plot on the right for V_P, blue dots represent the original Biot-Gassmann β_P function, and magenta dots represent the modified β_P function. Insets: histograms are for velocity values at depths less than 100 meters to emphasize the effect of the water table (practically no difference). For V_S, the blue curves represent the original water table, and the cyan curve represents the adjusted water table. For V_P, the blue curve represents the original β_P function with the original water table, the magenta curve represents the modified β_P function with the original water table, and the cyan curve represents the modified β_P with the adjusted water table.

inset histogram in the right-hand graph in fig. 5). This problem can be solved if β_P tends toward β_S as the saturation above the water table decreases toward 0 percent:

$$\beta_P = \beta_P S + \beta_S(1 - S). \tag{15}$$

Upon examining equations 7 and 8 and the effect of this condition on the V_P/V_S ratio, adopting equation 15 is equivalent to letting γ equal 1.

Water Table

One significant variable not yet introduced but readily apparent from the previous discussion is the depth to the water table and how saturation and pore pressure vary within the vadose zone and capillary fringe. As seen in figure 6, V_P/V_S ratios measured at relatively shallow (less than 1 km) depths can vary over a large range and increase to values of more than 10. This range of values is due to variations in porosity and the presence of material in the pore space with finite bulk modulus and no shear modulus. Higher porosities below the water table lead to higher V_P/V_S ratios. Above the water table, as fluid in the pore space is replaced with air, the bulk modulus decreases, and the V_P/V_S ratios return to values near 1.7.

In this work, the water-table model of Fan and others (2013) is used with modifications from observations of water levels in 10,597 wells across the United States available from the USGS National Water Information System (NWIS) and 1,575 wells in the greater Los Angeles area of southern California. Water-table depths range from 0 m near bodies of water to more than 100 m in much of the arid WUS (fig. 7). The information from the NWIS is available as a time series, which allows for a measure of seasonality and standard deviation. The median water-table depth observed in wells in the central and eastern United States, east of −100 degrees longitude, was 6 m with a standard deviation of 0.5 m. In the WUS (west of −100 degrees longitude), it was 26 m with a standard deviation of 1 m.

Above the water table, the capillary fringe is the lesser of 0.5 m or the depth to the water table. Above the capillary fringe lies the vadose zone, which is assumed to extend to the Earth's surface with a saturation S that follows half of a scaled sine wave from 0- to 100-percent saturation (for example, see fig. 9.4.1 in Bear [1972]):

$$S = \left[\frac{\sin\left(\pi\frac{d - d_V}{d_C - d_V} - \frac{\pi}{2}\right) + 1}{2}\right]^2, \tag{16}$$

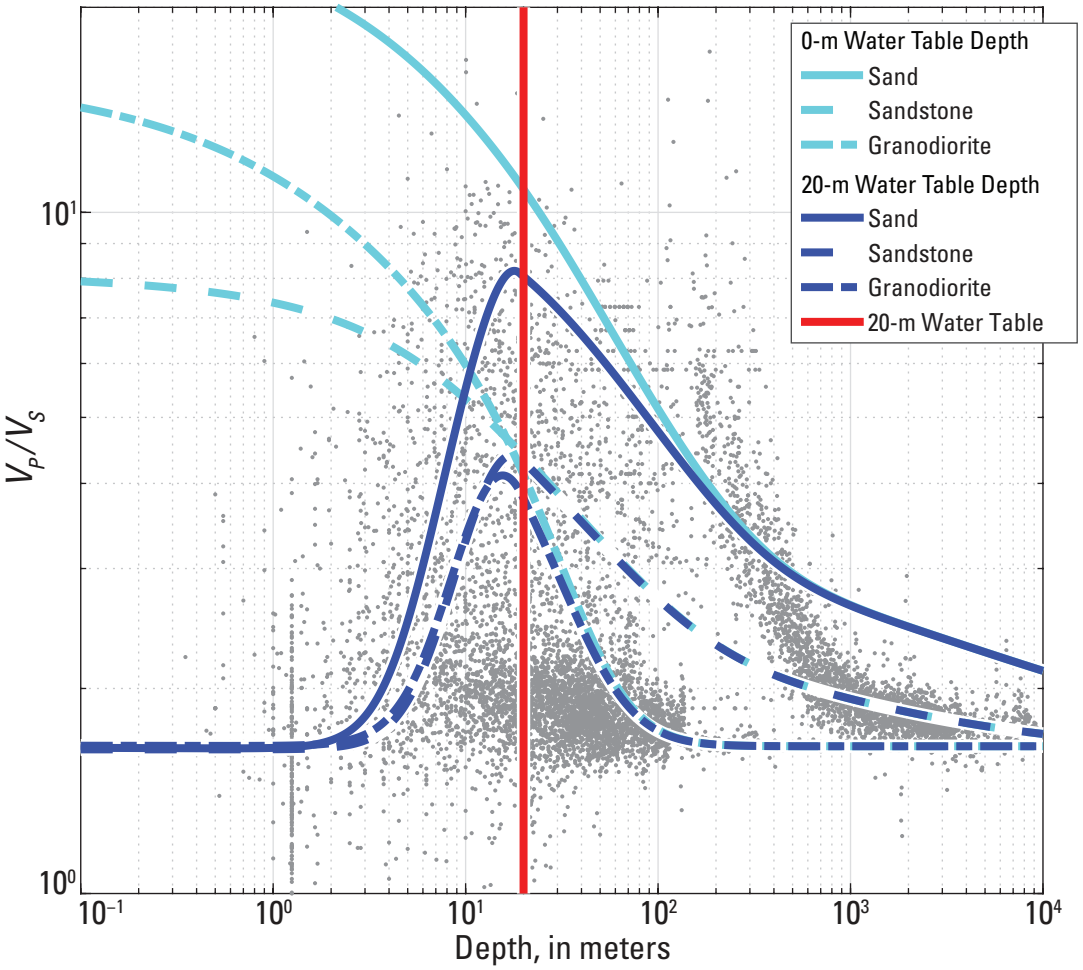

Figure 6. Observed V_P/V_S ratios versus depth (gray dots) as well as predicted relations for Quaternary sand (solid lines), Late Cretaceous sandstone (dashed lines), and Mesozoic granodiorite (alternating short and long dashes) with a water-table depth of 20 meters (m) (blue) and 0 m (cyan).

where d is depth, d_V is the depth to the top of the vadose zone, and d_C is the depth to the top of the capillary fringe. Fluid pressure within the vadose zone is taken from the formulation of Lu and others (2010) with parameters for sand ($a = 0.3$, $n = 3$):

$$P = -1000\frac{S}{a}\left(S^{\frac{n}{1-n}} - 1\right)^{\frac{1}{n}}. \quad (17)$$

With the porosity models for each lithology-age combination reported in the "Results" section, water-table values are further modified at velocity-profile locations in order to best match the observed V_P (cyan histograms in fig. 5*B*). This modification is done only for locations in the WUS that have both V_P and V_S with initial water-table depths greater than half of the depth of the first observed velocity value. The results are changes at 441 locations and an increase in the median water-table depth from 20 to 23 m, which is closer to the median of 26 m from the NWIS dataset for the WUS.

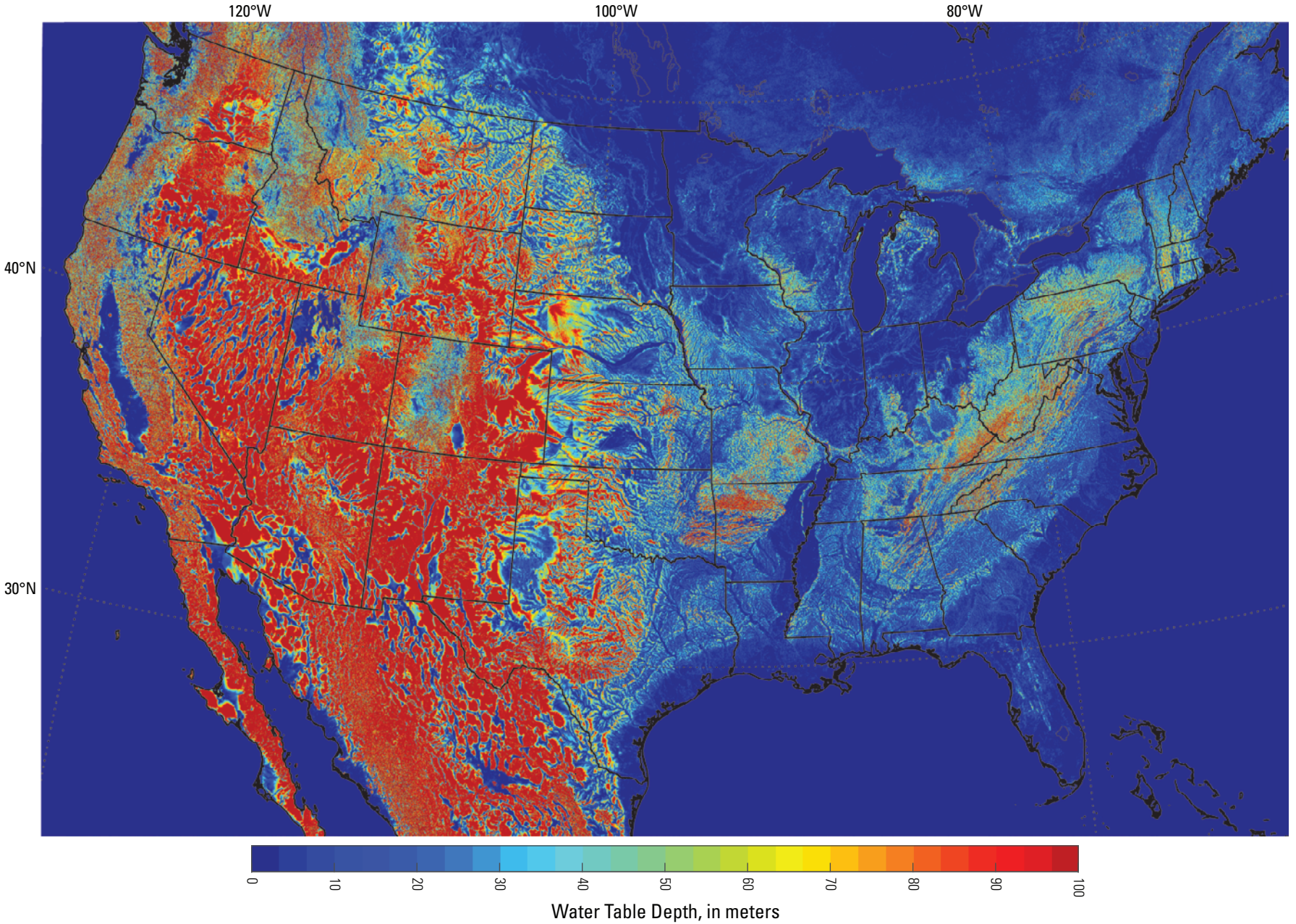

Figure 7. Water-table depths across the National Crustal Model.

Velocity Variability

The calibration presented here is a simplification of the actual conditions within the Earth. Geologic units have inherent variability in lithology and porosity. Water saturation within the porous rocks may be highly variable due to the volume of disconnected porosity, perched water tables, pumping, and other factors. Furthermore, predicting velocities can be hampered by imprecise knowledge of the subsurface geology, as indicated by the many adjustments described in the "Subsurface Geology" section as needed to calibrate this model.

If the geologic model is assumed to be known (from the adjustments made for calibration), and the B values for each layer within each profile and depth to water table are known (from the fitting during calibration), termed the ideal NCM, bias is less than 1 percent, and V_S predictions differ from observations with a standard deviation of 0.17 $\log_e$ units. V_P predictions will differ from observations with a standard deviation of 0.41 $\log_e$ units based on the initial water-table depths and will drop to 0.26 $\log_e$ units with the revised water-table depths. In many areas, however, no subsurface observations are available to adjust the geologic model and optimize the B value and depth to the water table. In this most general case, V_S is underpredicted by 4 percent, and V_P is overpredicted by 9 percent, on average. V_S and V_P predictions both differ from observations with a standard deviation of 0.58 $\log_e$ units. Regional variations, however, are significant and are discussed in the next section.

Comparison with Existing Geophysical Models

Regional velocity models have been constructed around Los Angeles (Kohler and others, 2003; Shaw and others, 2015) and San Francisco (Aagaard and others, 2010), California; Seattle, Washington (Stephenson and others, 2017); and Salt Lake City, Utah (Magistrale and others, 2008). These models make use of a host of information from tomography to reflection seismology to gravimetric studies to information obtained from boreholes.

In many cases, they convert V_P to V_S by assuming standard empirical relationships (Brocher, 2005b). For example, in the Bay Area, empirical V_P-depth relationships have been derived for 14 rock types and 2 locations (the Great Valley and La Honda Basin). V_S is derived from V_P by applying various rules, except for shallow Cenozoic sedimentary deposits (less than 40 m deep), which have their own unique V_S-depth relationship. The resulting V_P/V_S values are broadly consistent with those shown in figure 6 except that they do not explicitly account for porosity or the depth to the water table. Shallow V_P/V_S ratios in unsaturated sediments increase from a value of 2.5 at the surface to 4.0 at 40 m depth. At greater depths, V_P/V_S ratios in these units follow Castagna and others' (1985) "mudline," decreasing from almost 7 at 40-m depth to 2.5 at 500-m depth. In volcanic, igneous, and metamorphic rocks, V_P/V_S is derived from Brocher's (2005b) relation where V_P/V_S decreases from 4.5 at a V_P of 1.5 km/s to about 1.7 at a V_P greater than 5 km/s, with the exception of some lithologies that transition to the "mafic line" above about 4 km/s, which increases the V_P/V_S ratio.

In Seattle, a variety of generally non-overlapping V_P and V_S datasets were available, and conversions for most of the model domain were handled by using Brocher's (2005b) relations with exceptions for Cenozoic continental units. For Quaternary deposits with V_P determined from land-surface measurements and marine surveys, a V_P/V_S ratio of 2.5 at Earth's surface was assumed. This ratio was determined from time-averaged V_P and V_S values measured in the top 30 m of the Quaternary section. The ratio decreases linearly to a value of 2.2 at 1-km depth (the maximum thickness of Quaternary sediments) and drops to 2 in the underlying Tertiary sedimentary units (Stephenson and others, 2017).

Deviations between observed and modeled V_S for two southern California models (Kohler and others, 2003—model denoted as cvms426m01; Shaw and others, 2015—model denoted as cvmh1510), for which geophysical information was obtained by using the Southern California Earthquake Center's Unified Community Velocity Model software framework (Small and others, 2017), are relatively large, on average (fig. 8). These models include a geotechnical layer allowing for shear-wave velocities down to 100 m/s within tens of meters of the surface. With the application of detailed structural and geophysical information used to characterize the basins in and around Los Angeles, these models produce relatively reliable information about the basins but generally cannot reproduce details below shear-wave velocities of 1 km/s V_S outside of these basins. Hence, averaging over all locations where V_S is observed within their model domains, these models may overpredict V_S by a factor of 2, increasing from near 1 at

Figure 8 (following page). Shear-wave velocity (V_S; left), compressional-wave velocity (V_P; center), and density (ρ; right) misfit comparisons for several regions from Vancouver, British Columbia, to southern California. The red circles represent an ideal National Crustal Model (NCM), where the geology is assumed to be known; B values are fit to each lithology within each profile; and water-table depths are adjusted for four of the slowest profiles. Blue stars represent the NCM without refinement. Yellow squares represent the results from established geophysical models of the San Francisco Bay Area—(abbreviated as "bayarea") and southern California—(abbreviated as "cvmh" and "cvms426m01"). Polygons, the colored areas around the symbols, show the 5- to 95-percent regions in which the misfits lie. The dashed black line indicates the misfit of a profile with constant velocity or density. An ideal NCM is not shown for density misfits because the geologic profiles and B-values were not adjusted at these locations.

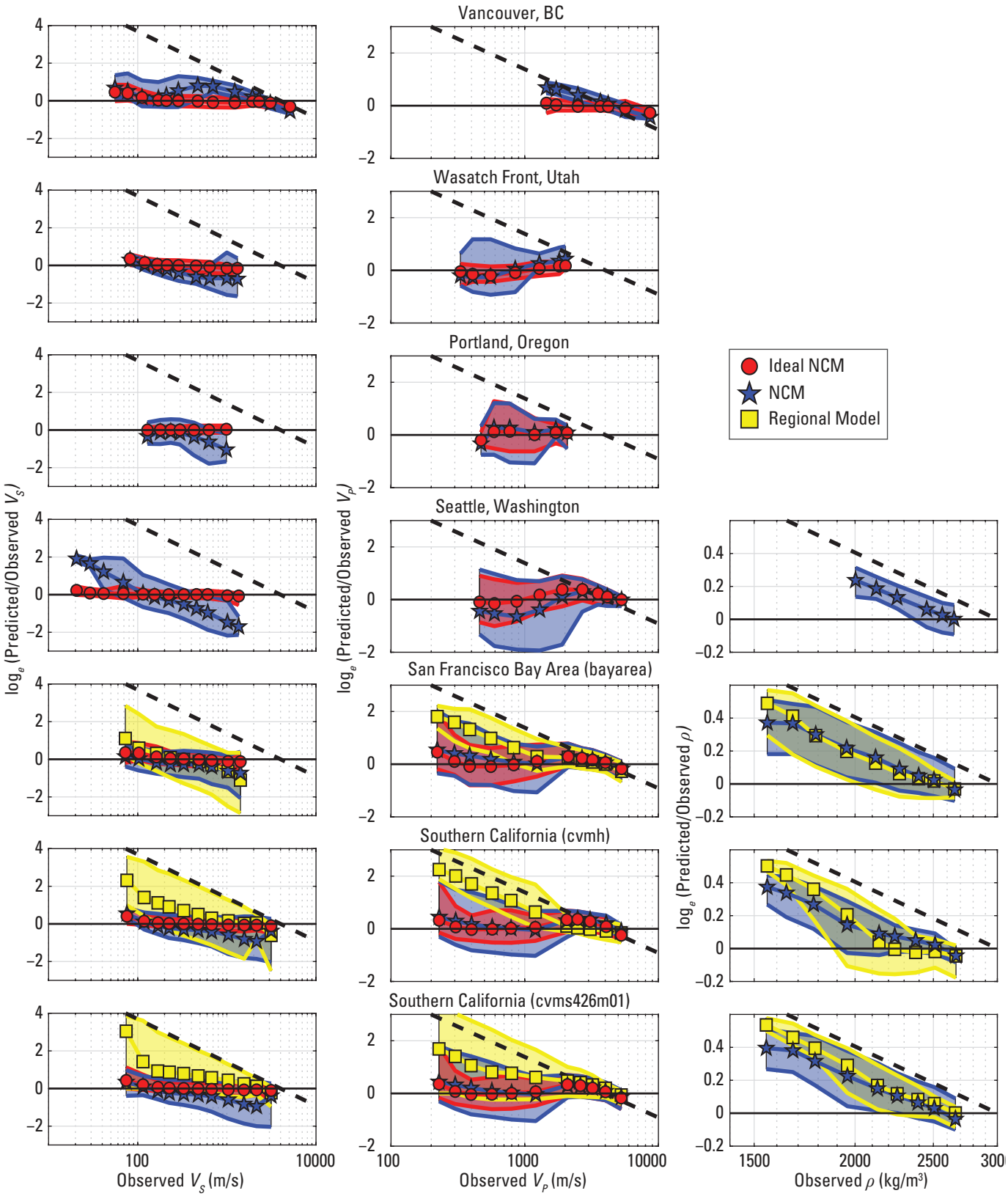
Vancouver, BC
Wasatch Front, Utah
Portland, Oregon
Seattle, Washington
San Francisco Bay Area (bayarea)
Southern California (cvmh)
Southern California (cvms426m01)
Ideal NCM
NCM
Regional Model
log$_e$ (Predicted/Observed V_S)
log$_e$ (Predicted/Observed V_P)
log$_e$ (Predicted/Observed ρ)
Observed V_S (m/s)
Observed V_P (m/s)
Observed ρ (kg/m^3)

about 2 km/s to more than a factor of 4 at 100 m/s. In contrast, resolution of the Bay Area model is more uniform with a high-resolution rectangular region surrounded by a lower resolution rectangular region. The model underpredicts the observations by only 5 percent on average but tends to deviate to the high side at V_S less than 300 m/s and to the low side at V_S greater than 300 m/s.

Investigating the NCM by region reveals important distinctions (fig. 8). Where the NCMGF is not fully developed to the northwest in Vancouver, British Columbia, the velocity profiles clearly indicate that the depth to bedrock and basement is too shallow in the NCMGF. This leads the NCM to overpredict V_S by as much as a factor of 2 between the bedrock and basement NCMGF transitions or between V_S values of about 200 and 2,000 m/s. In regions with a better developed NCMGF, important geologic contrasts need refinement, particularly within the Quaternary section. For example, the depth of the contact between the seismically slower Holocene lake and marine sediment and the underlying faster Pleistocene glacial drift in the Seattle area is probably shallower than the depth specified in the NCMGF, as inferred from the velocity profiles. The NCMGF without refinement leads to an underprediction of V_S above 100 m/s that progressively increases with increasing V_S. In the valleys of the Mojave Desert of southern California, the rapid increases of the observed V_S indicate that basement rock may be shallower than depicted in the NCMGF. This too leads to an underprediction of V_S, primarily between about 1 and 2 km/s.

Comparisons with V_P seem to tell a different story (fig. 8). All three California models tend to overpredict observed V_P for V_P values less than about 2 km/s. For the southern California models, this overprediction may be due to the use of the geotechnical layer (that is, the low-seismic velocity layer at and near the Earth's surface) only in the calculation of V_S. The zone above the water table may also exert some influence. In figure 6, V_P/V_S ratios drop to 1.7, but in the Bay Area model, for example, V_P/V_S ratios increase from 2.5 at the surface to 4 at 40 m depth. In the NCM, V_P is slightly overpredicted for the Bay Area and southern California, and in Seattle, below 2 km/s is a stronger underprediction. As is the case for V_S, the discrepancy in Seattle may be due to problems resolving the depth of important geologic contacts in the shallow surface.

All models tend to increasingly overestimate density as density decreases. Significant contributions to this misfit with regard to the NCM include but are not limited to the following three conditions:

1. A single set of constants that were used for m and α (equations 11 and 12). These constants are based on data for unconsolidated sands. Although estimates of density are much less biased for the alluvium and sandstones represented in this dataset, conceivably these constants likely differ by rock type. For example, a high-porosity limestone or basalt may have a relatively strong structural framework leading to a high seismic velocity but also relatively low density.
2. Another contributor could be problems with the NCMGF. Geologic assignments were not adjusted at the locations of density profiles, but a cursory comparison suggests that at one location in the southern Bay Area, the estimated depth to basement used in the NCMGF might be too shallow.
3. Finally, issues may relate to saturation. The NCM assumes 100-percent saturation below the water table, but pumping from confined aquifers will reduce saturation in these areas and thereby reduce both density and V_P.

The spread in V_S misfit between 5 and 95 percent of the median is relatively constant between about 2.5 and 3 $\log_e$ units for the cvmh1510 and Bay Area models and decreases steadily for cvms426m01 from about 4 at 100 m/s to less than 1 at 2 km/s. This steady decrease may have been caused by iterative tomographic methods that were used to refine the original model (Lee and others, 2014). The spread for the NCM without refinement peaks at almost 2.4 near 700 m/s, and drops to just under 0.5 at 3 km/s and down to 1.7 at 100 m/s. For the ideal NCM, where geology is assumed to be known and the B values and depth to water table are optimized for each profile, the spread decreases to about 0.5 for all values of V_S.

Deviations for the Seattle and Salt Lake City models were not investigated. The Seattle model available from ScienceBase (Stephenson, 2017) provides a model with only 500 m of vertical resolution, which is insufficient for comparison. In the Salt Lake City model, little to no deviation from the measured data probably exists because of the way in which the model was constructed. The Salt Lake City velocity model was built to honor borehole observations exactly within a specific distance of their locations, and the borehole data that were used to produce the Salt Lake City model were the only Salt Lake City observations used in this study. The initial Los Angeles model, designated as cvms (Kohler and others, 2003), was also built in this way but has since been modified by the use of other methods and additional data (Lee and others, 2014).

Discussion

Several primary uses for these existing models include earthquake simulations and maps of $Z_{1.0}$ and $Z_{2.5}$. Earthquake simulations have resulted in rich datasets which reveal the complexity of earthquake ground motions—for example, as seismic waves enter, are focused by, and reverberate within sedimentary basins. The simulations are expected to lead to far more accurate hazard analyses. Maps of $Z_{1.0}$ and $Z_{2.5}$, on the other hand, are used to calibrate GMMs. They are also applied to GMMs in hazard analyses for southern California, the Bay Area, and with modification in Puget Sound, Washington (Petersen and others, 2019).

Fortunately, the bias in shear-wave velocities below 1 km/s observed in existing California models may not be a problem. Earthquake simulations can require a minimum shear-wave velocity of 500 m/s because of computational limitations, and in the more populated basin areas where the Bay Area and Los Angeles models are better constrained, the bias above 500 m/s is not significant. Any potential bias is also not a problem for GMMs if the $Z_{1.0}$ or $Z_{2.5}$ map that was used to calibrate the GMM is the same map that is used in its application. As earthquake simulations become sensitive to lower velocities and as more of the velocity profile is used to construct site-amplification functions, however, greater attention will need to be given to the lowest velocities near the surface and to how rapidly velocities increase with depth.

Discrepancies between observed and predicted seismic velocity and density provide a roadmap for ways in which the NCM could be improved. For example, additional analysis is needed to better determine the variability of the dependences of porosity and elastic modulus on rock type. Another avenue of improvement relates to the NCMGF. Other geologic framework models, specifically hydrogeologic models (for example, Sweetkind and others, 2019, and references therein), have been developed for the WUS but have not been incorporated into the NCMGF. Furthermore, the underlying assumptions used to produce geologic structures within the NCMGF are not necessarily consistent with elements of the NCM. For example, the sedimentary-density profile used in gravity analysis of the Basin and Range Province of the WUS (Saltus and Jachens, 1995; Shah and Boyd, 2018) and from which the resulting bedrock- and basement-depth model is incorporated into the NCMGF, is based on a simple four-layer density structure in which the density of the sediments in the upper 200 m is 650 kilograms per cubic meter (kg/m^3) less than the density of the pre-Cenozoic basement. In contrast, the NCM, for example, predicts a density deficit of at least 800 kg/m^3 in the upper 200 m of Holocene alluvium in Las Vegas. If the density contrasts and gradients are greater than assumed in the gravity studies, the depths to bedrock and basement may be overestimated. Using the density-depth functions from the NCM with improved rock-dependent, elastic modulus-porosity relationships could lead to a more accurate NCMGF and resulting geophysical model.

Conclusions

A calibration of a porosity model for geologic units within the U.S. Geological Survey National Crustal Model (NCM) is presented to estimate shear-wave and compressional-wave velocities and densities as functions of depth, rock type, and rock age. Minor modifications to the Biot-Gassmann theoretical framework are needed to match observed low shear-wave and compressional-wave velocities above the water table. The resulting calibration yields an NCM that has little overall average bias between 100 meters per second and 3 kilometers per second shear-wave velocities; however, a strong regional variability in bias is due in part to imperfect knowledge of the subsurface geologic structure. Compressional-wave velocities have relatively low overall average and regional bias values between 200 meters per second and 5 kilometers per second, but uncertainty is greater at lower velocities due to imprecise knowledge of the depth to the water table and degree of saturation. On average, densities tend to be overpredicted, which may indicate unmodeled variability in the relationships between porosity and elastic modulus.

This calibration and the components of the NCM can be used in seismic hazard analyses by extracting the time-averaged shear-wave velocities in the upper 30 meters and the depths to 1.0 and 2.5 kilometers per second shear-wave velocity, which are parameters needed for current ground motion models. The NCM can also be used to produce more sophisticated site-response metrics or for earthquake simulations. Although the modeling of existing observations has been verified, the calibrations and components of the NCM have not been validated. The NCM will need to be validated for each of the aforementioned applications before a given product extracted from the NCM can be considered for policy decisions.

References Cited

Aagaard, B.T., Graves, R.W., Rodgers, A., Brocher, T.M., Simpson, R.W., Dreger, D., Petersson, N.A., Larsen, S.C., Ma, S., and Jachens, R.C., 2010, Ground motion modeling of Hayward fault scenario earthquakes, Part II—Simulation of long-period and broadband ground motions: Bulletin of the Seismological Society of America, v. 100, no. 6, p. 2945–2977.

Ahdi, S.K., Stewart, J.P., Ancheta, T.D., Kwak, D.Y., and Mitra, D., 2017, Development of VS profile database and proxy-based models for VS30 prediction in the Pacific Northwest region of North America: Bulletin of the Seismological Society of America, v. 107, no. 4, p. 1781–1801.

Bear, J., 1972, Dynamics of fluids in porous media: New York, American Elsevier, 764 p.

Boore, D., 2003, A compendium of P- and S-wave velocities from surface-to-borehole logging; summary and reanalysis of previously published data and analysis of unpublished data: U.S. Geological Survey Open-File Report 2003–191, 13 p., accessed June 15, 2019, at https://doi.org/10.3133/ofr03191.

Boyd, O.S., 2019, 3D geologic framework for use with the U.S. Geological Survey National Crustal Model, phase 1—Western United States: U.S. Geological Survey Open-File Report 2019–1081, 36 p. [Also available at https://doi.org/10.3133/ofr20191081.]

Boyd, O.S., 2020a, Calibration coefficients for the U.S. Geological Survey National Crustal Model and depth to water table: U.S. Geological Survey data release, https://doi.org/10.5066/P9GO3CP8.

Boyd, O.S., 2020b, Temperature model in support of the U.S. Geological Survey National Crustal Model for seismic hazard studies: U.S. Geological Survey Open-File Report 2019–1121, 15 p., accessed February 4, 2020, at https://doi.org/10.3133/ofr20191121.

Brocher, T.M., 2005a, A regional view of urban sedimentary basins in northern California based on oil industry compressional-wave velocity and density logs: Bulletin of the Seismological Society of America, v. 95, no. 6, p. 2093–2114, accessed March 1, 2017, at https://doi.org/10.1785/0120050025.

Brocher, T.M., 2005b, Empirical relations between elastic wavespeeds and density in the Earth's crust: Bulletin of the Seismological Society of America, v. 95, no. 6, p. 2081–2092.

Brocher, T.M., and Horta, E., 1998, Compilation of 19 sonic and density logs from 10 oil test wells in southwestern Oregon: U.S. Geological Survey Open-File Report 98–237, 38 p. [Also available at https://doi.org/10.3133/ofr98237.]

Brocher, T.M., and Ruebel, A.L., 1998, Compilation of 29 sonic and density logs from 23 oil test wells in western Washington State: U.S. Geological Survey Open-File Report 98–249, 60 p. [Also available at https://doi.org/10.3133/ofr98249.]

Brocher, T.M., Ruebel, A.L., Wright, T.L., and Okaya, D.A., 1998, Compilation of 20 sonic and density logs from 12 oil test wells along LARSE Lines 1 and 2, Los Angeles Region, California: U.S. Geological Survey Open-File Report 98–366, 54 p. [Also available at https://doi.org/10.3133/ofr98366.]

Castagna, J.P., Batzle, M.L., and Eastwood, R.L., 1985, Relationships between compressional-wave and shear-wave velocities in clastic silicate rocks: Geophysics, v. 50, p. 571–581.

Fan, Y., Li, H., and Miguez-Macho, G., 2013, Global patterns of groundwater table depth: Science, v. 339, no. 6122, p. 940–943.

Garrity, C.P., and Soller, D.R., 2009, Database of the Geologic Map of North America—Adapted from the map by J.C. Reed, Jr., and others (2005): U.S. Geological Survey Data Series 424, 7 p.

Gibbs, J.F., Fumal, T.E., Boore, D.M., and Joyner, W.B., 1992, Seismic velocities and geologic logs from borehole measurements at seven strong-motion stations that recorded the Loma Prieta earthquake: U.S. Geological Survey Open-File Report 92–287, 142 p.

Hashash, Y.M.A., Kottke, A.R., Stewart, J.P., Campbell, K.W., Kim, B., Moss, C., Nikolaou, S., Rathje, E.M., and Silva, W.J., 2014, Reference rock site condition for Central and Eastern North America: Bulletin of the Seismological Society of America, v. 104, no. 2, p. 684–701.

Kansas Geological Survey, 2017, LAS File Database, accessed February 19, 2017, at http://www.kgs.ku.edu/Magellan/Logs/.

Kohler, M.D., Magistrale, H., and Clayton, R.W., 2003, Mantle heterogeneities and the SCEC reference three-dimensional seismic velocity model version 3: Bulletin of the Seismological Society of America, v. 93, p. 757–774.

Lee, E., Chen, P., Jordan, T.H., Maechling, P.J., Denolle, M.A., and Beroza, G.C., 2014, Full-3-D tomography for crustal structure in Southern California based on the scattering-integral and the adjoint-wavefield methods: Journal of Geophysical Research, v. 119, no. 8, p. 6421–6451.

Lee, M.W., 2005, Proposed moduli of dry rock and their application to predicting elastic velocities of sandstones: U.S. Geological Survey Scientific Investigations Report 2005–5119, 14 p., accessed September 5, 2019, at https://doi.org/10.3133/sir20055119.

Lee, M.W., 2010, Predicting S-wave velocities for unconsolidated sediments at low effective pressure: U.S. Geological Survey Scientific Investigations Report 2010–5138, 13 p., accessed June 4, 2019, at https://doi.org/10.3133/sir20105138.

Lu, N., Godt, J.W., and Wu, D.T., 2010, A closed-form equation for effective stress in unsaturated soil: Water Resources Research, v. 46, issue 5, 14 p., accessed January 25, 2018, at https://doi.org/10.1029/2009WR008646.

Magistrale, H., Olsen, K., and Pechmann, J., 2008, Construction and verification of a Wasatch Front community velocity model—Collaborative research with San Diego State University and the University of Utah—Final technical report: Reston, Va., U.S. Geological Survey report, prepared by San Diego State University and the University of Utah under contracts 05HQGR0006, 05HQGR0011, 06HQGR0009, and 06HQGR0012, 14 p., accessed February 27, 2020, at https://earthquake.usgs.gov/cfusion/external_grants/reports/05HQGR0006.pdf.

Mavko, G., and Mukerji, T., 1998, Bounds on low-frequency seismic velocities in partially saturated rocks: Geophysics, v. 63, no. 3, p. 918–924.

Mooney, W.D., 2013, Database of Central and Eastern North American (CENA) Seismic Velocity Structure (Task 2 of USGS-NRC Work Agreement 2011–2014): United States Nuclear Regulatory Commission, Agencywide Documents Access and Management System (ADAMS) accession number ML14280A412, 231 p., accessed February 27, 2020, at https://adams.nrc.gov/wba/.

Mustard, P.S., and Rouse, G.E., 1994, Stratigraphy and evolution of the Tertiary Georgia Basin and subjacent Upper Cretaceous sedimentary rocks, southwestern British Columbia and northwestern Washington State, *in* Monger, J.W.H., ed., Geology and geological hazards of the Vancouver region, southwestern British Columbia: Geological Survey of Canada Bulletin 481, p. 97–169, accessed August 2, 2019, at https://doi.org/10.4095/203244.

Pelletier, P., Broxton, D., Hazenberg, P., Zeng, X., Troch, P.A., Niu, G.-Y., Williams, Z., Brunke, M.A., and Gochis, D., 2016, A gridded global data set of soil, immobile regolith, and sedimentary deposit thicknesses for regional and global land surface modeling: Journal of Advances in Modeling Earth Systems, v. 8, issue 1, p. 41–65, accessed June 26, 2017, at https://doi.org/10.1002/2015MS000526.

Petersen, M.D., Shumway, A.M., Powers, P.M., Mueller, C.S., Moschetti, M.P., Frankel, A.D., Rezaeian, S., McNamara, D.E., Luco, N., Boyd, O.S., Rukstales, K.S., Jaiswal, K.S., Thompson, E.M., Hoover, S.M., Clayton, B.S., Field, E.H., and Zeng, Y., 2019, 2018 update of the U.S. National Seismic Hazard Model—Overview of model and implications: Earthquake Spectra, v. 36, issue 1, p. 5–41. [Also available at https://doi.org/10.1177%2F8755293019878199.]

Saltus, R.W., and Jachens, R.C., 1995, Gravity and basin-depth maps of the Basin and Range Province, Western United States: U.S. Geological Survey Geophysical Investigation Map 1012, 1 pl., scale 1: 2,500,000, accessed January 18, 2020, at https://doi.org/10.3133/gp1012.

Shah, A.K., and Boyd, O.S., 2018, Depth to basement and thickness of unconsolidated sediments for the western U.S.—Layers of the USGS National Crustal Model, version 1.0: U.S. Geological Survey Open-File Report 2018–1115, 13 p. [Also available at https://doi.org/10.3133/ofr20181115.]

Shaw, J.H., Plesch, A., Tape, C., Suess, M.P., Jordan, T.H., Ely, G., Hauksson, E., Tromp, J., Tanimoto, T., Graves, R., Olsen, K., Nicholson, C., Maechling, P.J., Rivero, C., Lovely, P., Brankman, C.M., and Munster, J., 2015, Unified structural representation of the southern California crust and upper mantle: Earth and Planetary Science Letters, v. 415, p. 1–15, accessed March 17, 2017, at https://doi.org/10.1016/j.epsl.2015.01.016.

Shi, J., and Asimaki, D., 2018, A generic velocity profile for basin sediments in California conditioned on VS30: Seismological Research Letters, v. 89, no. 4, p. 1397–1409, accessed May 23, 2018, at https://doi.org/10.1785/0220170268.

Small, P., Gill, D., Maechling, P.J., Taborda, R., Callaghan, S., Jordan, T.H., Ely, G.P., Olsen, K.B., and Goulet, C.A., 2017, The SCEC Unified Community Velocity Model software framework: Seismological Research Letters, v. 88, no. 5., p. 1530–1552, accessed December 1, 2017, at https://doi.org/10.1785/0220170082.

Sowers, T., and Boyd, O.S., 2019, Petrologic and mineral physics database for use with the USGS National Crustal Model: U.S. Geological Survey Open-File Report 2019–1035, 17 p. [Also available at https://doi.org/10.3133/ofr20191035.]

Stephenson, W.J., 2017, Data for P- and S-wave seismic velocity models incorporating the Cascadia subduction zone for 3D earthquake ground motion simulations—Update for Open-File Report 2007–1348: U.S. Geological Survey data release, accessed December 1, 2019, at https://doi.org/10.5066/F7NS0SWM.

Stephenson, W.J., Odum, J.K., Williams, R.A., McBride, J.H., and Tomlinson, I., 2012, Characterization of intrabasin faulting and deformation for earthquake hazards in southern Utah Valley, Utah, from high-resolution seismic imaging: Bulletin of the Seismological Society of America, v. 102, no. 2, p. 524–540, accessed February 28, 2017, at https://doi.org/10.1785/0120110053.

Stephenson, W.J., Reitman, N.G., and Angster, S.J., 2017, P- and S-wave velocity models incorporating the Cascadia subduction zone for 3D earthquake ground motion simulations, version 1.6—Update for Open-File Report 2007–1348: U.S. Geological Survey Open-File Report 2017–1152, 17 p., accessed September 25, 2018, at https://doi.org/10.3133/ofr20171152.

Sweetkind, D., Graymer, R., Higley, D., and Boyd, O., 2019, Status of three-dimensional geological mapping and modelling activities in the U.S. Geological Survey, chap. 26 *of* MacCormack, K.E., Berg, R.C., Kessler, H., Russell, H.A.J., and Thorleifson, L.H., eds., 2019, 2019 synopsis of current three-dimensional geological mapping and modelling in geological survey organizations: Alberta Energy Regulator/Alberta Geological Survey AER/AGS Special Report 112, p. 278–289, accessed January 18, 2020, at https://ags.aer.ca/publications/SPE_112.html.

Voigt, W., 1928, Lehrbuch der kristallphysik [Textbook of crystal optics]: Vieweg+Teubner Verlag, 978 p.

Yong, A., Thompson, E.M., Wald, D., Knudsen, K.L., Odum, J.K., Stephenson, W.J., and Haefner, S., 2016, Compilation of VS30 data for the United States: U.S. Geological Survey Data Series 978, 8 p., accessed June 28, 2017, at https://doi.org/10.3133/ds978.

Zimmer, M.A., 2003, Seismic velocities in unconsolidated sands—Measurements of pressure, sorting, and compaction effects: Stanford, Calif., Stanford University, Ph.D. dissertation, 204 p.

ISSN 2331-1258 (online)
https://doi.org/10.3133/ofr20201052